

# Connecting Anti-integrability to Attractors for Three-Dimensional, Quadratic Diffeomorphisms

Amanda E. Hampton and James D. Meiss\*

Department of Applied Mathematics

University of Colorado

Boulder, CO 80309-0526

Amanda.Hampton@colorado.edu James.Meiss@colorado.edu

May 11, 2023

## Abstract

We previously showed that three-dimensional quadratic diffeomorphisms have anti-integrable (AI) limits that correspond to a quadratic correspondence; a pair of one-dimensional maps. At the AI limit the dynamics is conjugate to a full shift on two symbols. Here we consider a more general AI limit, allowing two parameters of the map to go to infinity. We prove the existence of AI states for each symbol sequence for three cases of the quadratic correspondence: parabolas, ellipses and hyperbolas. A contraction argument gives parameter domains such that this is a bijection, but the correspondence also is observed to apply more generally. We show that orbits of the original map can be obtained by numerical continuation for a volume-contracting case. These results show that periodic AI states evolve into the observed periodic attractors of the diffeomorphism. We also continue a periodic AI state with a symbol sequence chosen so that it continues to an orbit resembling a chaotic attractor that is a 3D version of the classical 2D Hénon attractor.

## Contents

<b>1</b>	<b>Introduction</b>	<b>2</b>
<b>2</b>	<b>Two-Parameter Anti-integrable Limit</b>	<b>4</b>
<b>3</b>	<b>Existence of AI states</b>	<b>6</b>
3.1	One-to-One Correspondence . . . . .	6
3.2	Numerical Verification of AI States . . . . .	8
<b>4</b>	<b>Analytical Bounds</b>	<b>8</b>
4.1	Parabolic Case . . . . .	10
4.2	Elliptical Case . . . . .	11
4.3	Hyperbolic Case . . . . .	12

---

\*The authors were supported in part by NSF grant DMS-181248 and a donation from Northrup Grumman. Useful conversations with Yi-Chiuan Chen are gratefully acknowledged.

<b>5</b>	<b>Strongly Contracting Case</b>	<b>13</b>
5.1	Low-Period Orbits and the Period-Doubling Cascade . . . . .	15
5.2	Hénon-like Attractors . . . . .	18
<b>6</b>	<b>Conclusions</b>	<b>19</b>
<b>A</b>	<b>Backwards Map</b>	<b>23</b>
<b>B</b>	<b>Parabolic Case: Two Iterates</b>	<b>23</b>
<b>C</b>	<b>Continuation Algorithm</b>	<b>24</b>

# 1 Introduction

While dynamical systems can have *simple* behavior when they are integrable, they can also behave relatively simply at a complementary limit, where they are anti-integrable (AI) [AA90]. For the former, all orbits lie on invariant tori determined by a complete set of invariants of the system, and for the latter all orbits are represented by a Bernoulli shift on a finite set of symbols—a pure form of chaos. Indeed, just as one can continue from an integrable system to one that is nearly integrable to find persistent tori using KAM theory, one can also continue from an AI limit to find chaotic dynamics, under an assumed nondegeneracy condition [MM92, Aub95, SM98]. These two methods, while fundamentally different, can both help elucidate the more difficult, intermediate case where their can be a complex mixture of both regular and chaotic motion.

In this paper we continue our application of these ideas to the study of quadratic diffeomorphisms [HM22b, HM22a]. Our work is based on a similar analysis for the 2D Hénon map [SM98, SDM99, DMS05, Che06], but extended to three-dimensional quadratic diffeomorphisms [LM98]. These quadratic maps have a two-symbol AI limit, and upon continuation, each symbol sequence becomes an orbit of the deterministic map. The simplest continuation argument uses the contraction mapping theorem, but numerical methods can continue these orbits beyond the parameter regions that the theorem applies.

Anti-integrability in higher-dimensional systems, written as scalar difference equations, has also been developed by [DLM06, LM06, JLM08, LM10] and has been used to extend [MM92] to more general multi-dimensional cases [CL15]. We compared our approach to these ideas in [HM22b]. Our goal in the current paper is to extend these arguments to a more general anti-integrable limit that includes two limiting parameters.

We study the 3D quadratic diffeomorphism  $L : \mathbb{R}^3 \rightarrow \mathbb{R}^3$  with quadratic inverse which, as was shown in shown in [LM98, LLM99], can be written in the form

$$\begin{aligned}
 L(x, y, z) &= (\delta z + \alpha + \tau x - \sigma y + Q(x, y), x, y), \\
 Q(x, y) &\equiv ax^2 + bxy + cy^2.
 \end{aligned}
 \tag{1}$$

The orbits of (1) are sequences  $\{(x_t, y_t, z_t) : t \in \mathbb{Z}\}$  that satisfy

$$(x_{t+1}, y_{t+1}, z_{t+1}) = L(x_t, y_t, z_t).$$

The map has seven parameters  $(\alpha, \tau, \sigma, a, b, c)$ , and  $\delta = \det DL$ , the Jacobian determinant. The volume-preserving case,  $\delta = 1$ , is as a normal form near a fixed point with a triple-one multiplier [DM08]. The volume-contracting case,  $|\delta| < 1$ , arises as a normal form near homoclinic bifurcations [GMO06] and can give rise to discrete Lorenz-like attractors [GGKS21].

We introduce the convention described in [LM98]: assuming  $a + b + c \neq 0$  and  $2a + b \neq 0$ , then an affine coordinate transformation allows one to set

$$a + b + c = 1 \text{ and } \tau = 0. \quad (2)$$

We adopt this simplification so the map only depends on  $(\alpha, \sigma, a, c)$ , and the Jacobian  $\delta$ .<sup>1</sup>

Following [HM22b], to set up the anti-integrable limit, first rewrite (1) as a third-order difference equation for  $\{x_t : t \in \mathbb{Z}\}$  upon noting that  $y_{t+1} = x_t$  and  $z_{t+1} = x_{t-1}$ ,

$$x_{t+1} = \delta x_{t-2} + \alpha - \sigma x_{t-1} + Q(x_t, x_{t-1}). \quad (3)$$

It is convenient to then rescale the phase space variables, defining  $\xi_t = \varepsilon x_t$ , thus introducing a parameter  $\varepsilon$ . Then, using (2), (3) becomes

$$\begin{aligned} 0 &= \mathcal{L}_\varepsilon(\xi_{t+1}, \xi_t, \xi_{t-1}, \xi_{t-2}) \\ &= Q(\xi_t, \xi_{t-1}) + \varepsilon^2 \alpha - \varepsilon(\xi_{t+1} + \sigma \xi_{t-1} - \delta \xi_{t-2}). \end{aligned} \quad (4)$$

Generally a difference equation like (4) has an AI limit if it degenerates in some way—say to a lower-order equation, such that it is no longer a deterministic map. Such a limit is useful if (a) the orbits at the AI limit can be simply characterized (for example by symbolic dynamics), and (b) if each such orbit can be shown to continue away from the limit (for example by a contraction mapping argument or by numerical continuation). This is the method introduced in [SM98] for the Hénon map, that we extended in [HM22b] for (4).

To get such a limit we will assume that  $a, b, c$  are “structural” parameters that remain finite and that  $|\delta| \leq 1$  so that the map is not volume expanding. Different AI limits can be categorized by scaling the remaining parameters  $\alpha$  and  $\sigma$  with  $\varepsilon$  so that the third-order difference equation (4) degenerates to a lower-order, non-deterministic system at  $\varepsilon = 0$ . In [HM22b], the parameter  $\varepsilon$  was defined by  $\alpha \varepsilon^2 = 1$ . In this case  $\varepsilon \rightarrow 0$  corresponds to the anti-integrable limit  $\alpha \rightarrow -\infty$ . Here we will allow two parameters to be unbounded:  $\alpha \rightarrow -\infty$  and  $\sigma \rightarrow \pm\infty$ . Setting

$$\alpha = -\varepsilon^{-2}, \quad \sigma = r\varepsilon^{-1}, \quad (5)$$

so that  $\sigma^2/\alpha = -r^2$  is finite, results in the difference equation

$$\mathcal{L}_\varepsilon(\xi_{t+1}, \xi_t, \xi_{t-1}, \xi_{t-2}) = Q(\xi_t, \xi_{t-1}) - r\xi_{t-1} - 1 - \varepsilon(\xi_{t+1} - \delta\xi_{t-2}), \quad (6)$$

When  $\varepsilon = 0$ , (6) degenerates to

$$Q(\xi_t, \xi_{t-1}) = r\xi_{t-1} + 1, \quad (7)$$

The implication is that sequential points must lie on a quadratic curve, which is determined by the discriminant,

$$\Delta \equiv b^2 - 4ac. \quad (8)$$

---

<sup>1</sup>If  $c = 1$  and  $a = b = 0$ , then it would be more appropriate to assume  $b + 2c \neq 0$  and set  $\sigma = 0$ .

For  $\Delta < 0$ , (7) defines an ellipse in the  $(\xi_{t-1}, \xi_t)$ -plane,  $\Delta = 0$  gives a parabola, and  $\Delta > 0$ , a hyperbola. Note that when  $\Delta = -4ac = ar^2$ , the curve (7) becomes degenerate in the sense that the parabola turns into a pair of parallel lines, the hyperbola becomes two intersecting lines, and the ellipse becomes a single point. The discriminant will play a crucial role in the analysis presented in §2.

For the remainder of our discussion we assume  $a \neq 0$  and set  $b = 0$ , so that  $a = 1 - c$  and  $\Delta = -4ac$  now only depends on the value of  $c$ . A proof is given in §3 for the existence of AI states, which uses a similar contraction mapping argument found in [HM22b], but results in a larger parameter region. The remainder of §3 gives numerical results for the region of existence of AI states in  $(r, c)$ -space. In §4 we will see that this region appears to converge to a simpler one that we compute analytically. We present details of the computation of this analytical region for the three classes of quadratic curve.

In §5 we focus on a “strongly contracting” case, where  $\delta = 0.05$ , that we also studied in [HM22a]. Since the Jacobian determinant is small, the orbits of this map are close to those of a Hénon map that (1) reduces to at  $\delta = 0$ . In [HM22a] we found periodic, regular aperiodic, and chaotic Hénon-like attractors for this case for regions in  $(\alpha, \sigma)$ . The resonances that correspond to periodic attractors mimic the Arnold-tongues seen for circle maps and the “shrimps” seen in two parameter families of 1D maps [Gal94, MT87, FOG13]. In §5, we redo these computations using the parameters  $(\alpha, r)$ .

We then continue the AI states away from  $\varepsilon = 0$ , to see how, at least for low periods, they evolve into the observed attractors. In each case we see that the attractor can be attributed to an orbit that connects to the AI limit—supporting the “no-bubbles” conjecture of [SDM99]. Lastly, the continuation method is used to find periodic approximations to a Hénon-like attractor. The resulting AI state for the periodic approximation continues to an orbit that is a good approximation of the attractor.

## 2 Two-Parameter Anti-integrable Limit

When  $b = 0$ ,  $a = 1 - c$  and (7) becomes

$$a\xi_t^2 + c\xi_{t-1}^2 = r\xi_{t-1} + 1, \quad (9)$$

a quadratic curve symmetric about the horizontal axis and centered at

$$\xi^o = \frac{r}{2c}. \quad (10)$$

The discriminant reduces to  $\Delta = 4c(c - 1)$ , so this quadratic curve is simply determined by the value of  $c$ :

$$\begin{aligned} \text{Ellipse: } \Delta < 0 &\implies 0 < c < 1 \\ \text{Parabola: } \Delta = 0 &\implies c = 0 \text{ and } c = 1 \\ \text{Hyperbola: } \Delta > 0 &\implies c < 0 \text{ and } c > 1 \end{aligned} \quad (11)$$

In the  $(r, c)$  plane these correspond to the regions sketched in Fig. 1: blue for ellipses, tan for hyperbolas, and the bounding black lines for parabolas. Recall that  $\Delta = -4ac = ar^2$  leads to degeneracies. Here, there are three cases: when  $c = 1 - a = 1$ , (9) becomes a pair of vertical lines (recall that we assume  $a \neq 0$ , though we do consider the  $a = 0$  case for the backwards map); when

$c = -\frac{r^2}{4}$ , (9) becomes a pair of intersecting lines; and finally when  $c = r = 0$ , a pair of horizontal lines. In Fig. 1 these are the red, dashed curves. Finally, insets in this figure show examples of the quadratic curve (9) in each  $(r, c)$  region or boundary.

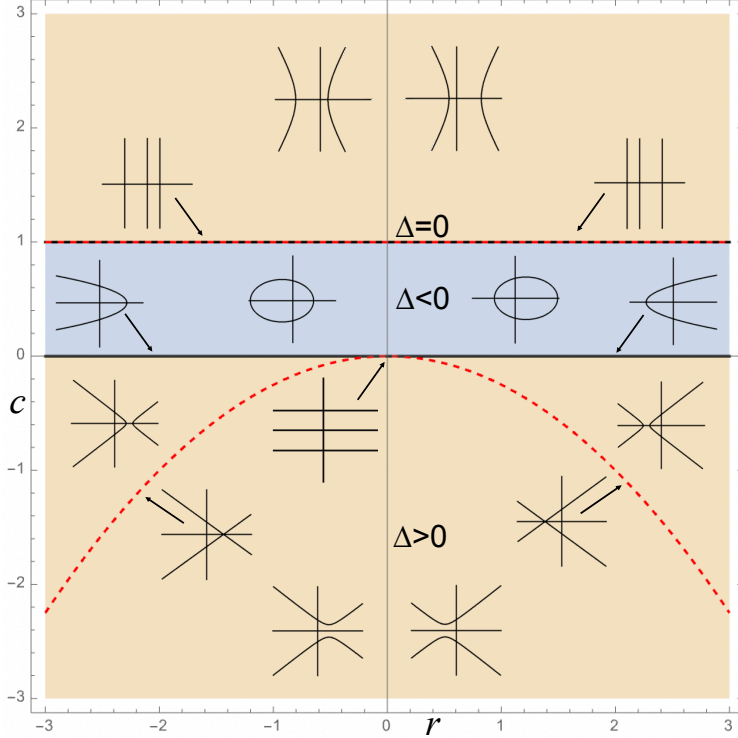


Figure 1: Regions in the  $(r, c)$ -plane that correspond with the AI curve (7) classification: elliptic (blue) with  $\Delta < 0$ , hyperbolic (tan) with  $\Delta > 0$ , and parabolic (black lines) with  $\Delta = 0$ . The red-dashed curves correspond to degeneracies. Insets are included of the curve (7) to show what type of curve (7) corresponds to with different  $(r, c)$ -values.

An AI state is a sequence  $\{\xi_t : t \in \mathbb{Z}\}$  that lies on the curve (7) for all  $t \in \mathbb{Z}$ . Since the map (1) is three-dimensional, the curve (7) represents a surface in  $\mathbb{R}^3$ . This relation must hold for all  $t$ . Therefore, if the axes are labeled as  $(\xi_{t-1}, \xi_t, \xi_{t+1})$ , AI states must lie on the intersection of the two surfaces

$$\{Q(\xi_t, \xi_{t-1}) = r\xi_{t-1} + 1\} \cap \{Q(\xi_{t+1}, \xi_t) = r\xi_t + 1\}.$$

For example, when  $\Delta < 0$  this is the intersection of two elliptical cylinders [HM22b].

Dynamically, (9) can be thought of as a non-deterministic quadratic correspondence, and its solutions, provided they exist, are AI states. These can be obtained by solving (9) for  $\xi_t$ , giving a pair of 1D maps:

$$\xi_t = f_{s_t}(\xi_{t-1}) = s_t \sqrt{\frac{-c\xi_{t-1}^2 + r\xi_{t-1} + 1}{a}}, \quad s_t \in \{-, +\}, \quad (12)$$

since we have assumed  $a \neq 0$ .<sup>2</sup>

<sup>2</sup>If  $a = 0$  the set (9) is a pair vertical lines at the fixed points (14) and an AI state is simply a sequence of these

If the radicand of (12) is strictly positive, either choice  $s_t = \pm$  is valid, and each point  $\xi_{t-1}$  has two images defined by the branches,  $f_-$  and  $f_+$ , respectively. Note that  $f_+ \geq 0$  and  $f_- \leq 0$  and the maps are symmetric,  $f_-(\xi_{t-1}) = -f_+(\xi_{t-1})$ . Consequently, whenever  $\xi_t \neq 0$  is an AI state, it has a unique symbol sequence

$$s = \{\dots s_0, s_1, s_2 \dots\} \in \Sigma \equiv \{-, +\}^\infty, \quad (13)$$

so that  $s_t = \text{sign}(\xi_t)$  represents the branch of (7) at time  $t$ . For example, the fixed points of (12) correspond to the symbol sequences  $s = \{+\}^\infty$  and  $\{-\}^\infty$ , and are

$$\{\pm\}^\infty : \xi_\pm = \frac{1}{2}(r \pm \sqrt{r^2 + 4}). \quad (14)$$

When  $r = 0$ , a case we previously studied [HM22a], the fixed points are simply the symbol sequence themselves, i.e.,  $\xi_t = s_t$ . Fixed points exist for any  $(r, c)$ , and are the unique orbits with the symbol sequences  $\{+\}^\infty$  and  $\{-\}^\infty$ .

### 3 Existence of AI states

In this section, we will extend the results of [HM22b] to the case  $r \neq 0$  for (9) on the existence and uniqueness of AI states. In order that a point has a forward orbit under the relation (12), it is sufficient for the range to be a subset of the domain. In addition, so that each AI state have an unambiguous symbol sequence, we require that the image not include the origin. This is equivalent to requiring the radicand of (12) to be strictly positive. Thus we suppose there exists a set  $B \subset \mathbb{R}$  so that

$$f_\pm(B) \subset B \setminus \{0\}. \quad (15)$$

The correspondence between symbol sequences and AI states becomes bijective when the derivative,

$$f'_{s_t}(\xi_{t-1}) = \frac{s_t(r - 2c\xi_{t-1})}{2\sqrt{a(-c\xi_{t-1}^2 + r\xi_{t-1} + 1)}}. \quad (16)$$

has magnitude less than one on  $B$ . Indeed, when  $B$  is compact, as we noted in [HM22b], the contraction mapping theorem implies this bijection: for each  $s \in \Sigma$  there is a unique  $\{\xi_t\} \in B^\infty$  satisfying (12).

In §3.1 we generalize this result, requiring only that the  $n$ -step composition has an absolute slope less than one for some  $n \in \mathbb{N}$ . This allows for points of the orbit to lie on portions of the curve (9) with a ‘steeper’ slope, thus increasing the parameter regime where we can prove the existence of AI states. In §3.2 we compute the  $n$ -step bounds numerically.

#### 3.1 One-to-One Correspondence

Suppose that  $B \subset \mathbb{R}$  is compact, and that  $\xi = \{\dots \xi_{-1}, \xi_0, \xi_1, \dots\}$  denotes a sequence in

$$\mathcal{B} = B^\infty \subset \mathbb{R}^\infty, \quad (17)$$

---

points  $\xi_t = \xi_\pm$ .

the countable product of  $B$ . Define  $\mathcal{F} : \mathcal{B} \times \Sigma \rightarrow \mathcal{B}$  by

$$\mathcal{F}_t(\xi; s) = f_{s_t}(\xi_{t-1}), \quad (18)$$

for each  $s \in \Sigma$  (13) and  $t \in \mathbb{Z}$ . Note that any fixed point of  $\mathcal{F}$  is an orbit of (12) with sequence  $s$ . More generally, for each  $k \in \mathbb{N}$ , let  $\mathcal{F}^k : \mathcal{B} \times \Sigma \rightarrow \mathcal{B}$  denote the  $k^{\text{th}}$  iterate,

$$\mathcal{F}_t^k(\xi, s) = f_{s_t} \circ f_{s_{t-1}} \circ \dots \circ f_{s_{t-k+1}}(\xi_{t-k})$$

For example, if  $s$  is a period- $k$  symbol sequence (e.g.,  $s_{t+k} = s_t, \forall t \in \mathbb{Z}$ ) and  $\xi$  is a period- $k$  orbit of (12), then it is a fixed point of  $\mathcal{F}^k$ .

Lastly, for  $n \in \mathbb{N}$ , define the set of parameters

$$\mathcal{R}_n^+ = \{(r, c) : \exists B \neq \emptyset, f_{s_t}(B) \subset B, \|D\mathcal{F}^n\|_\infty < 1\}, \quad (19)$$

where

$$\|D\mathcal{F}^n\|_\infty = \max_{s_0, s_1, \dots, s_{n-1}} \sup_{x \in B} \left| \frac{d}{dx} (f_{s_{n-1}}(f_{s_{n-2}}(\dots(f_{s_0}(x))\dots))) \right|, \quad (20)$$

i.e., the  $\infty$ -norm on  $\mathcal{B} \times \Sigma$ . A simple extension of the result in [HM22b] is the following.

**Lemma 1.** *Given  $(r, c) \in \mathcal{R}_n^+$  and  $\xi \in \mathcal{B}$ , there is a one-to-one correspondence between each sequence  $s \in \Sigma$  and state  $\{\xi\} \subset \mathcal{B}$  satisfying (12).*

*Proof.* Consider a pair of sequences  $\xi, \eta \in \mathcal{B}$ . Given some  $s \in \Sigma$  and  $\mathcal{F}$  (18), the fixed points of  $\mathcal{F}$  are orbits of the map (12). Since  $B$  is a compact subset of  $\mathbb{R}$ , and  $\mathcal{B}$  is complete in the  $\ell^\infty$  norm. Then

$$\|\mathcal{F}^n(\xi) - \mathcal{F}^n(\eta)\|_\infty \leq \|D\mathcal{F}^n\|_\infty \|\xi - \eta\|_\infty,$$

so that for parameters in  $\mathcal{R}_n^+$ ,  $\mathcal{F}^n$  is a contraction. Thus  $\mathcal{F}^n$  has a unique fixed point  $\xi^* = \mathcal{F}^n(\xi^*)$ .

When  $(r, c) \in \mathcal{R}_n^+$ ,  $f_{s_t}(B) \subset B$ ; therefore, for each  $s \in \Sigma$ , there is an  $\eta^* \in \mathcal{B}$  such that for each  $t \in \mathbb{Z}$ ,  $\mathcal{F}_t(\eta^*, s) = \eta_t^*$ , since this is simply an orbit of the 1D map (12). Since  $\eta^* = \mathcal{F}(\eta^*)$ , clearly we also have  $\eta^* = \mathcal{F}^n(\eta^*)$ . Since the fixed point of  $\mathcal{F}^n$  is unique,  $\eta^* = \xi^*$ . Hence, each symbol sequence has a unique corresponding orbit of (12).

Note that, by construction, the conditions  $(r, c) \in \mathcal{R}_n^+$  and  $\xi \in B$  guarantee that the radicand of (12) is strictly positive, implying that every state of (12) has a unique symbol sequence  $s \in \Sigma$ . Therefore, there exists a one-to-one correspondence between symbol sequences and states of (12).  $\square$

Additionally, when  $c \neq 0$ , the argument of Lem. 1 can be applied using the backwards map,

$$\xi_{t-1} = g_{s_t}(\xi_t) = \frac{1}{2c} \left( r + s_t \sqrt{r^2 + 4c - 4ac\xi_t^2} \right), \quad (21)$$

which is obtained by solving (9) for  $\xi_{t-1}$ . Given a similar region,  $\mathcal{R}_n^-$ , to (19), defined using (21), the proof of a one-to-one correspondence is the same as that for Lem. 1.

### 3.2 Numerical Verification of AI States

Of course, it can be a nontrivial task to compute the regions  $\mathcal{R}_n^\pm$  required for Lem. 1. Here we will assume that the set  $B$  which satisfies (19) is a closed interval:

$$B = [-\beta, \beta]. \quad (22)$$

Though this is probably not necessary, it makes the calculations simpler. The specific choices for  $\beta$  depend on  $\Delta$  and will be given below in §4. Anticipating these results, we will compute in this section the region  $\mathcal{R}_n^\pm$  in the  $(r, c)$  plane where (20) is achieved for  $n$  up to 15.

Figure 2(a) shows the results of computations for a grid of  $500^2$  parameter points in the region  $|r| \leq 3$  and  $|c| \leq 3$ . For each  $(r, c)$  point, 100 initial conditions along  $B$  are iterated  $n$  times using  $f_{s_t}$  (12) for  $\mathcal{R}_n^+$  or  $g_{s_t}$  (21) for  $\mathcal{R}_n^-$ . This is done for each of the  $2^n$  possible symbol sequences  $\{s_1, s_2, \dots, s_n\} \in \{+, -\}^n$  for  $n \leq 15$ . For each iteration the derivative (20) is estimated as the maximum over the grid of orbits and the set of symbols. If  $\|D\mathcal{F}^n\|_\infty < 1$ , then the parameters are added to the region  $\mathcal{R}_n^\pm$ . The results, shown in Fig. 2(a), have a maximum of  $n = 12$  forward steps, and  $n = 14$  backward steps (i.e., using  $g_\pm$ ). The enlargement, in Fig. 2(b), shows similar results on a  $500^2$  parameter grid for  $|r| \leq 1.17$  and  $-0.35 \leq c \leq 0.75$ , with a maximum of  $n = 15$  steps in each direction. In each case the color scale gives the number of forward iterates for  $\mathcal{R}_n^+$  (yellow to green) and backward iterates for  $\mathcal{R}_n^-$  (cyan to magenta). The white region in the figures corresponds to parameters for which the bound on the derivative is never attained. Of course, the regions are necessarily nested:  $\mathcal{R}_{n-1}^\pm \subset \mathcal{R}_n^\pm$ . Moreover, as  $n$  grows the enlargement of the regions becomes relatively small and they seem to converge. We will say more about this in the next section.

Note that most of the  $(r, c)$  values in the regions shown in Fig. 2(a) correspond to the hyperbolic case, either  $c > 1$  for  $\mathcal{R}_n^-$  where the hyperbola is more *vertical* or  $c < -r^2/4$  for  $\mathcal{R}_n^+$  where the hyperbola is more *horizontal*. That the slopes should be small for the backwards or forward map, respectively, in these cases can also be seen in the insets in Fig. 1. It is more delicate to satisfy the conditions for Lem. 1 for the elliptic case,  $0 < c < 1$ ; indeed, for an ellipse the slope is necessarily zero or infinite at the vertices, and so  $B$  must be more carefully selected to avoid these points.

## 4 Analytical Bounds

In this section, we report results for the parameters  $(r, c)$  that *only* satisfy the condition (15), the simplest requirement so that each point has a forward or backward orbit as well as an unambiguous symbol sequence. We denote these sets by

$$\begin{aligned} \mathcal{R}_A^+ &\equiv \{(r, c) : f_s(B) \subset B \setminus \{0\}, s \in \{+, -\}\}, \\ \mathcal{R}_A^- &\equiv \{(r, c) : g_s(B) \subset B \setminus \{0\}, s \in \{+, -\}\}, \end{aligned} \quad (23)$$

using the forward map (12) and the backward map (21), respectively. We will again assume that  $B$  is a closed interval of the form (22).

The results will be obtained in the following subsections for the three classes of quadratic curves:



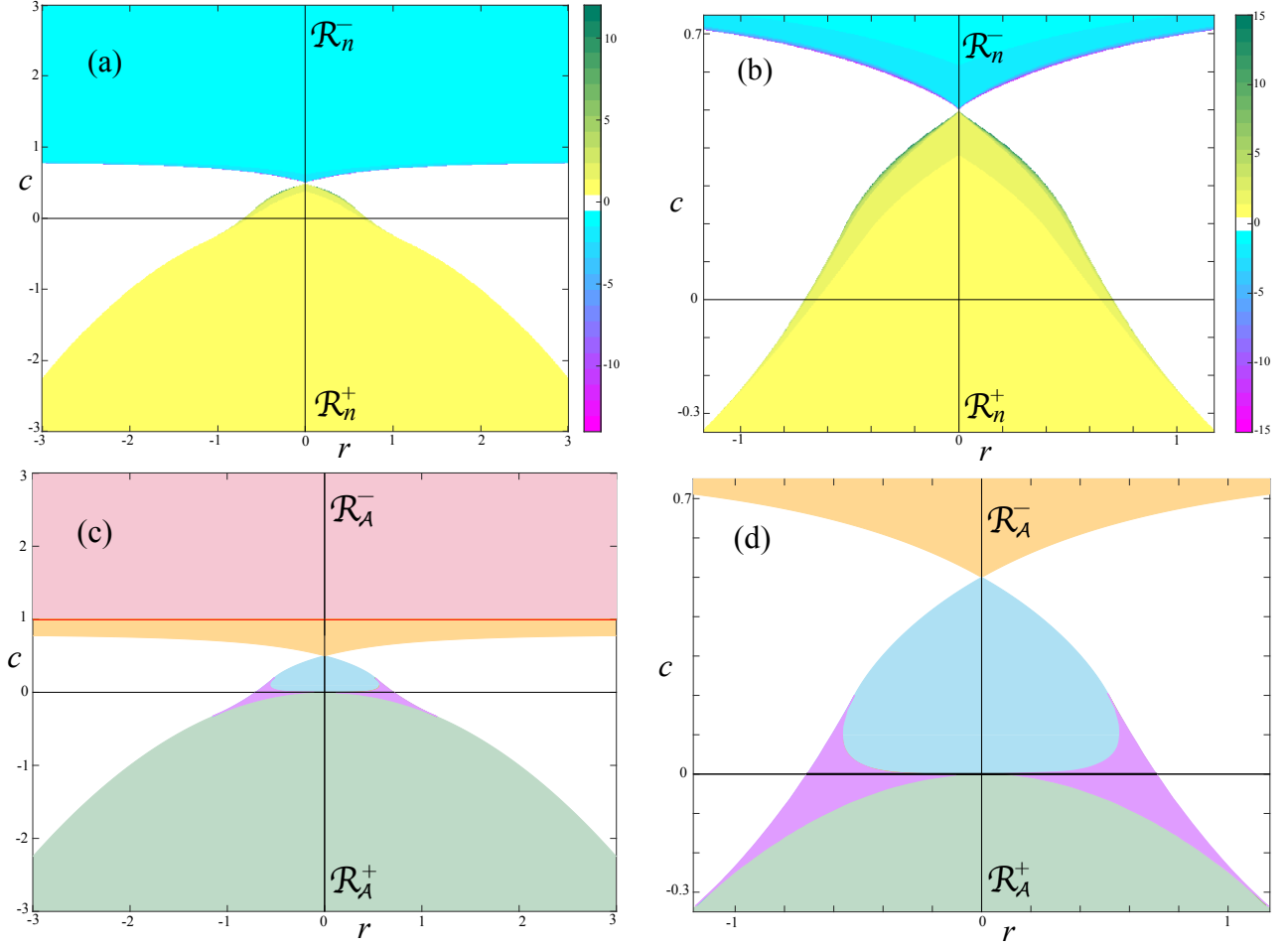


Figure 2: (a) Numerically computed approximations to  $\mathcal{R}_n^\pm$ . Colors correspond with the number of forward (yellow to green) or backward (cyan to magenta) iterates that are used. The maximum number of steps is  $n = 12$  for the forward direction and 14 for the reverse direction. (b) An enlargement of (a) about the origin where  $|r| \leq 1.17$  and  $-0.35 \leq c \leq 0.75$ , for  $n$  up to 15 in either direction. (c) The analytical regions  $\mathcal{R}_A^\pm$  (24) in the  $(r, c)$  plane so that  $f_s(B) \subset B$ . for (12). Colors correspond with the different  $\Delta$ -cases described in the subsections of §3.2: hyperbolic (red for  $c > 1$ , green, and purple for  $c < 0$ ), elliptic (tan, blue, and purple for  $0 < c < 1$ ) and parabolic (an interval along  $c = 0$  and  $c = 1$ ). (d) An enlargement of (c) using the same bounds as (b).

parabolas, ellipses, and hyperbolas. These calculations lead to the forms

$$\begin{aligned}
 \mathcal{R}_A^+ &= \left\{ (r, c) : |r| \leq \frac{2}{\sqrt{15}}, c < \mathcal{C}_2(r) \right\} \cup \left\{ (r, c) : \frac{2}{\sqrt{15}} \leq |r| \leq \frac{2}{\sqrt{3}}, c < 1 + |r|(|r| - \sqrt{r^2 + 4}) \right\} \\
 &\quad \cup \left\{ (r, c) : |r| \geq \frac{2}{\sqrt{3}}, c < -\frac{r^2}{4} \right\}, \\
 \mathcal{R}_A^- &= \{(r, c) : c > \mathcal{C}_3(r)\}
 \end{aligned} \tag{24}$$

Here, the functions  $\mathcal{C}_i(r)$  are roots of the cubic polynomial

$$P(c) = 64c^3 + 32(r^2 - 2)c^2 + (r^2 - 4)(5r^2 - 4)c - 4r^4; \tag{25}$$

these are real when  $|r| < 2\sqrt{2}/5$ . The calculations for  $\mathcal{R}_{\mathcal{A}}^-$  are summarized Appendix A.

The regions (24) are shown in Fig. 2(c) and (d). They include subsets of the hyperbolic case (red for  $c > 1$ , green, and purple for  $c < 0$ ), the elliptic case (tan, blue, and purple for  $0 < c < 1$ ) and the parabolic case (an interval along  $c = 0$  and  $c = 1$ ).

Comparing the upper and lower panels of Fig. 2, it appears that the numerically found regions  $\mathcal{R}_n^+$  and  $\mathcal{R}_n^-$  converge onto the analytically determined regions (24) as  $n$  grows. To verify this we computed Hausdorff distances between  $\mathcal{R}_n^\pm$  and  $\mathcal{R}_{\mathcal{A}}^\pm$ , listed in Table 1 as a function of  $n$ . Here we compare the sets on the domain  $(r, c) = [0, \frac{2}{\sqrt{3}}] \times [-\frac{1}{3}, \frac{4}{5}]$ , using a  $500^2$  grid. This region is chosen to take advantage of symmetry  $r \rightarrow -r$ .

n	$\ \mathcal{R}_n^+ - \mathcal{R}_{\mathcal{A}}^+\ _H$	$\ \mathcal{R}_n^- - \mathcal{R}_{\mathcal{A}}^-\ _H$
1	0.112941	0.113266
2	0.020430	0.015774
5	0.014207	0.012091
10	0.008460	0.007873
15	0.007008	0.006532

Table 1: Hausdorff distances between the sets  $\mathcal{R}_n^\pm$  and  $\mathcal{R}_{\mathcal{A}}^\pm$  for increasing  $n$ . For larger  $n$ , the distances decrease, as is confirmed visually in Fig. 2.

Since the distances in Table 1 appear to go to zero, it seems reasonable to infer the following:

**Conjecture 2.** *As  $n \rightarrow \infty$ , the  $\mathcal{R}_n^\pm$  converges to  $\mathcal{R}_{\mathcal{A}}^\pm$ .*

Note that (15) requires the strict inequalities  $f_+ > 0$  and  $f_- < 0$  so that each orbit has a uniquely defined symbol sequence, i.e., that  $f_+(B) \cap f_-(B) = \emptyset$ . Since the range must be a strict subset of the domain, successive iterates give nested sets:  $B \supset f_\pm(B) \supset f_\pm(f_\pm(B)) \dots$ . The AI states lie within the resulting Cantor-like sets.

## 4.1 Parabolic Case

In this section we compute the regions (23) for the parabolic case,  $\Delta = 0$ . Since we assume  $b = 0$ , this requires that  $(a, c) = (0, 1)$  or  $(1, 0)$ . When  $a = 0$ , the curve (9) degenerates to a pair of vertical lines at the fixed points,  $\xi_\pm$ , (14). For this case, the forward map is not defined, and one must use the backwards map, (21), see Appendix A.

For the case  $c = 0$ , the parabola (9) has a vertex at  $(-\frac{1}{r}, 0)$  when  $r \neq 0$  and opens in the positive (negative)  $\xi_{t-1}$  direction when  $r > 0$  ( $r < 0$ ), recall the sketches in Fig. 1. When  $r = 0$ , the parabola degenerates to a pair of horizontal lines and  $f_\pm(\xi) = \xi_\pm$ , (14).

Since the interval  $B$  must contain the fixed points, as these are orbits with  $s = \{+\}^\infty$  and  $\{-\}^\infty$ , and it must contain the images  $f_\mp(\xi_\pm) = -\xi_\pm$ , we define  $B$  using the maximum absolute fixed point  $\beta = \xi_{max}$ , where

$$\xi_{max} = \max(|\xi_+|, |\xi_-|) = \frac{1}{2}(|r| + \sqrt{r^2 + 4}). \quad (26)$$

Since each branch is monotone on  $B$ , it is clear that  $f_\pm(B) \subset B$ . To guarantee that the radicand of (12) is positive, the vertex of the parabola must be outside  $B$ ; i.e.  $-1/r < -\beta$ , this requires  $|r| < \frac{1}{\sqrt{2}}$ . This gives

$$\{(r, 0) : |r| < \frac{1}{\sqrt{2}}\} \subset \mathcal{R}_{\mathcal{A}}^+.$$

This is depicted in Fig. 2(d) as the thicker, black line segment.

It's also easy to find the region  $\mathcal{R}_1^+$ , where  $|f'_\pm(\xi)| < 1$  when  $\xi \in B$ . Using (16),  $|f'_\pm(\xi)| = 1$  at  $\xi = \frac{r}{4} - \frac{1}{r}$ , this requires that this value is outside  $B$ , or equivalently

$$16 - 40r^2 + 5r^4 > 0 \implies |r| < \sqrt{\frac{1}{5}(20 - 8\sqrt{5})} \approx 0.6498394.$$

Note that this segment is only 10% smaller than that for  $\mathcal{R}_A^+$ . We extend this computation to compute  $\mathcal{R}_2^+$  in Appendix B; this gives  $|r| < 0.6984177$ , now only about 1% smaller than that for  $\mathcal{R}_A^+$ . These values agree with the numerical results of Fig. 2(b) along  $c = 0$ . For the calculations used to obtain the values in Table 1 (i.e. numerical results for  $\mathcal{R}_{15}^+$ ), the interval is  $|r| \leq 0.7057789$ , a mere 0.2% smaller than  $\mathcal{R}_A^+$ . For the figure the grid size is  $2.314(10)^{-3}$  so that the next grid point is  $r = 0.70809$ , which is outside  $\mathcal{R}_A^+$ ; thus the computed interval is the optimal.

## 4.2 Elliptical Case

When  $0 < c < 1$ , the curve (9) is an ellipse centered at (10) and contained in the rectangle

$$\left[ \frac{1}{2c}(r - \sqrt{r^2 + 4c}), \frac{1}{2c}(r + \sqrt{r^2 + 4c}) \right] \times \left[ -\sqrt{\frac{r^2 + 4c}{4ac}}, \sqrt{\frac{r^2 + 4c}{4ac}} \right]. \quad (27)$$

There are two cases to consider. First, if the interval  $[-\xi_{max}, \xi_{max}]$  (26) contains the center of the ellipse (10), i.e., if

$$|\xi^o| < \xi_{max}, \quad (28)$$

then, since  $B$  must include the fixed points, (15) requires that the vertical range of the ellipse must be a subset of  $B$ , see the sketch in Fig. 3(a). Indeed for this case we can take (22) with  $\beta$  equal to top of the rectangle (27). Requiring the range to be a strict subset of the domain gives the condition

$$\beta < \frac{1}{2c}(-|r| + \sqrt{r^2 + 4c}).$$

After some algebra, this implies that

$$\left\{ (r, c) : |r| < \frac{2\sqrt{2}}{5}, \mathcal{C}_1(r) < c < \mathcal{C}_2(r) \right\} \subset \mathcal{R}_A^+, \quad (29)$$

where  $\mathcal{C}_{1,2}(r)$  are the smaller two roots of the cubic polynomial (25). The discriminant of this polynomial,  $2^8 r^2 (r^2 + 4)^4 (8 - 25r^2)$ , is positive when  $|r| < 2\sqrt{2}/5$ , and in this case it has three positive, real roots. This is the blue region in Fig. 2(c) and (d).

When (28) is not satisfied, the region defined by the fixed points does not contain the top or bottom vertices of the ellipse; thus the slope of  $f_+$  in the set  $[-\xi_{max}, \xi_{max}]$ , (26), is always positive. An example is shown in Fig. 3(b). For this case, as for the parabola, we can use  $\beta = \xi_{max}$  for the interval (22). In order that  $\{0\} \notin f_\pm(B)$ , the horizontal vertices of the ellipse must be outside  $B$ ; this gives the condition

$$\frac{-|r| + \sqrt{r^2 + 4c}}{2c} > \frac{1}{2}(|r| + \sqrt{r^2 + 4}). \quad (30)$$

Some more algebra then gives the additional region

$$\left\{ (r, c) : \frac{2}{\sqrt{15}} < |r| < \frac{1}{\sqrt{2}}, 0 < c < 1 + |r|(|r| - \sqrt{r^2 + 4}) \right\} \subset \mathcal{R}_A^+.$$

In Fig. 2 (c) and (d), this additional portion in  $0 < c < 1$  is colored purple. The backwards case,  $\mathcal{R}_A^-$ , is treated in Appendix A, and results in the tan region in Fig. 2 (c) and (d).

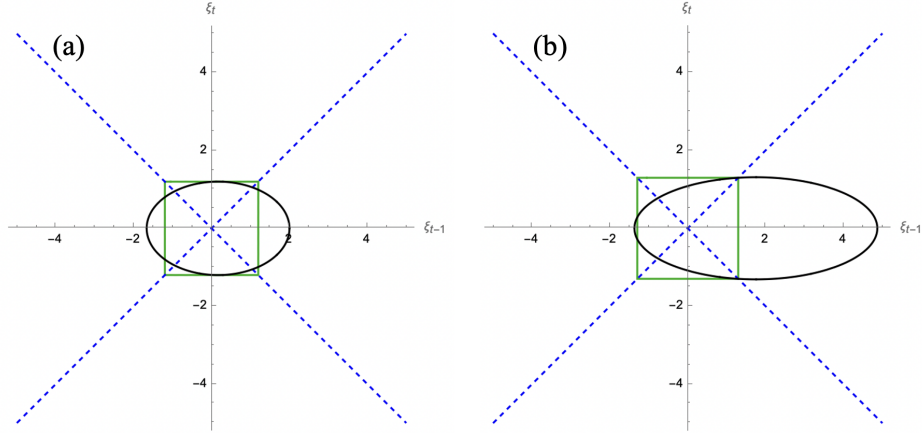


Figure 3: Elliptical curves for parameters (a)  $(r, c) = (0.1, 0.3)$  and (b)  $(r, c) = (0.525, 0.15)$ . The box  $B^2$  is shown in green, and the diagonals  $\xi_t = \pm\xi_{t-1}$  are dashed blue.

### 4.3 Hyperbolic Case

For the hyperbolic case  $\Delta < 0$ . Since  $a = 1 - c$  this implies that  $c < 0$  or  $c > 1$ . Supposing first that

$$c < -\frac{r^2}{4}, \quad (31)$$

then the branches of the hyperbola are graphs over  $\xi_{t-1}$ , see the sketch in Fig. 4(a). In this case, we can take  $B = [-\xi_{max}, \xi_{max}]$ , defined by (26). The images of  $B$  then satisfy (15). The implication is that

$$\left\{ (r, c) : c < -\frac{r^2}{4} \right\} \subset \mathcal{R}_{\mathcal{A}}^+.$$

This region is pictured in green in Fig. 2(c) and (d).

In addition, note that the asymptotes of the hyperbola are the lines

$$\xi_t = \pm \sqrt{\frac{c}{c-1}} \left( \xi_{t-1} - \frac{r}{2c} \right). \quad (32)$$

Consequently when  $c < 0$  the magnitude of these slopes is less than one. Moreover, since (31) implies that the branches are graphs over  $\xi_{t-1}$  these slopes bound those of  $f_{\pm}$  on  $B$ . Thus, by Lem. 1 for  $n = 1$ , there is a one-to-one correspondence between AI states and symbol sequences whenever (31) is satisfied.

When  $-r^4/4 < c < 0$ , the branches of hyperbola are graphs over  $\xi_t$ , as sketched in Fig. 4(b). In this case, the domain omits the open interval

$$\left( \frac{1}{2c}(r - \sqrt{r^2 + 4c}), \frac{1}{2c}(r + \sqrt{r^2 + 4c}) \right),$$

between the vertices. This set must be disjoint from  $B$  in order that the maps  $f_{\pm}$  be well-defined. The vertices are outside  $[-\xi_{max}, \xi_{max}]$  under the same condition (30) found in the elliptic case. This implies that

$$\left\{ (r, c) : \frac{1}{\sqrt{2}} \leq |r| \leq \frac{2}{\sqrt{3}}, -\frac{r^2}{4} < c < 1 + |r|(|r| - \sqrt{r^2 + 4}) \right\} \subset \mathcal{R}_{\mathcal{A}}^+.$$

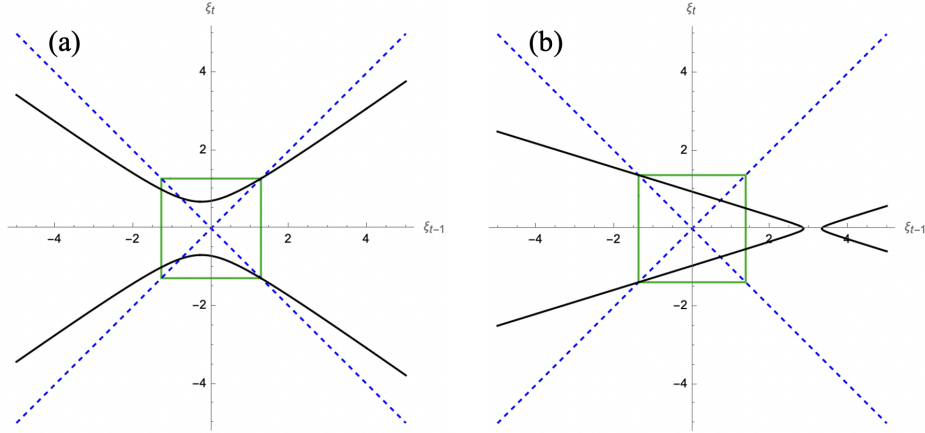


Figure 4: Hyperbolic curves for parameters (a)  $(r, c) = (0.5, -1)$ , (b)  $(r, c) = (-0.65, -0.105)$ . The box  $B^2$  is shown in green, and the diagonals  $\xi_t = \pm\xi_{t-1}$  are dashed blue.

This region is pictured in purple for  $c < 0$  in Fig. 2(a) and (d).

Note that condition (30) is never achieved when  $c > 1$ ; a subset of this case becomes  $\mathcal{R}_A^-$  and is treated in Appendix A.

## 5 Strongly Contracting Case

The map (1) is volume preserving when  $\delta = 1$ , and projects to a two-dimensional Hénon map in  $(x, y)$  when  $\delta = 0$ .<sup>3</sup> In this section, we study orbits for a “strongly contracting case”, setting

(SC) Strongly Contracting:  $(a, c, \delta) = (1, 0, 0.05)$ .

We studied this case previously in [HM22b] for  $r = 0$ ; this corresponds to the AI limit  $\alpha \rightarrow -\infty$ , with  $\sigma$  finite. There we found a number of periodic attractors, many of which undergo period-doubling bifurcations as  $\alpha$  decreases. We also found chaotic attractors with a 3D horseshoe-like structure, reminiscent of the Hénon attractor.

Here we generalize these results to look at the effect of  $r \neq 0$ . Note that since  $a = 1$  and  $c = 0$ , the quadratic curve at the AI limit is a parabola. When  $|r| < 2^{-1/2}$ , the results of §4.1 imply that there is a one-to-one correspondence between symbol sequences and AI states for this case.

Characteristics of the attractors for (SC) over a region in  $(\alpha, r)$  are shown in Fig. 5. These are found by iterating the difference equation (3), upon setting  $\sigma = r\varepsilon^{-1} = r\sqrt{-\alpha}$  under the assumption that  $\alpha < 0$ . For each  $(\alpha, r)$  on a  $1500^2$  grid, we choose the initial point  $(x_0, x_{-1}, x_{-2}) = (x_-, x_-, x_-) + (0.001, 0, 0)$ , where

$$x_- = \frac{1}{2} \left( 1 + \sigma - \delta - \sqrt{(1 + \sigma - \delta)^2 - 4\alpha} \right),$$

<sup>3</sup>For example, the classic Hénon attractor is found when  $(\alpha, \sigma, \delta) = (-1.4, -0.3, 0)$ , or equivalently  $(\varepsilon, r) \approx (0.84515, -0.2535)$  [HM22b, Appendix].

is a fixed point of (3) This point is iterated forward  $T = 5000$  times to eliminate transients. An orbit is declared divergent if, for some  $t \leq T$ ,  $|x_t| > \kappa_{max}^4$ , for  $\kappa_{max} = 3.26724$  in Fig. 5(a), and  $\kappa_{max} = 2.28343$  in Fig. 5(b). Such divergent cases are colored white in Fig. 5. If the orbit remains bounded, we detect low periods by iterating up to 90 more steps, checking for a close return: the approximate period,  $p$ , is the smallest time for which

$$\|x_{T+p} - x_T\| < 10^{-4}.$$

Orbits with these periods are colored according to the color map shown in Fig. 5. For the remaining parameter values we label the orbit as regular (black) or chaotic (grey) by computing the approximate maximal Lyapunov exponent as described in [HM22a]. Thus, the colors of Fig. 5 indicate the type of attractor expected for each  $(\alpha, r)$ .

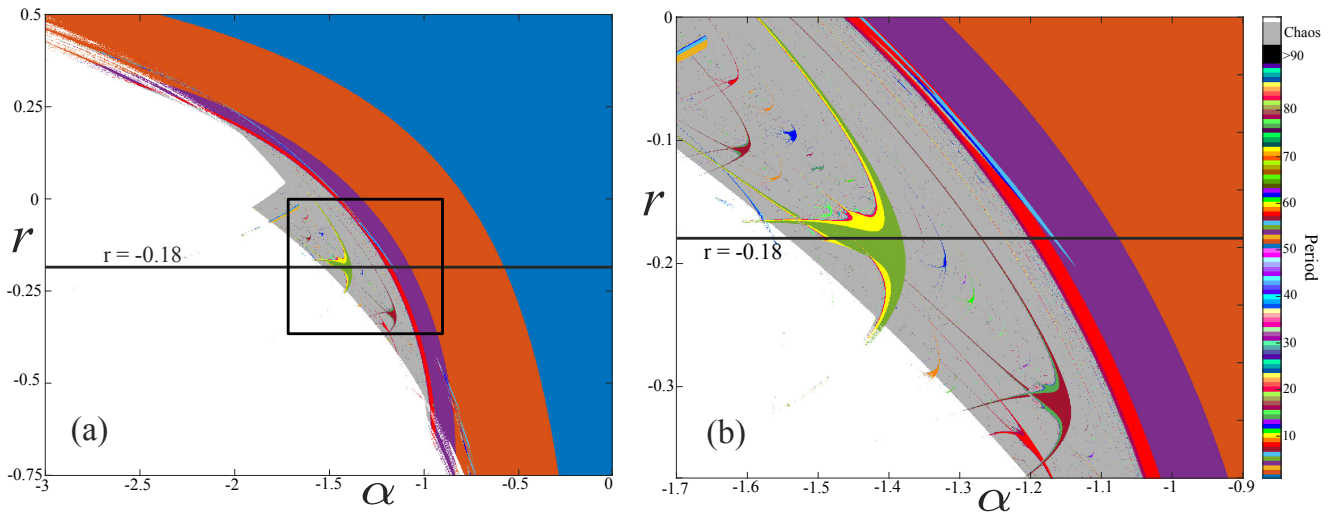


Figure 5: (a) Bounded, periodic and chaotic orbits for a strongly contracting case of map (1) with parameters (SC). The color scale indicates the period with chaotic orbits colored gray and unbounded orbits white. If the orbit is bounded, not chaotic, but not identified as having period at most 90, the point is black. Also pictured is a line segment at  $r = -0.18$ . (b) An enlargement of the boxed region in (a) around the period-five shrimp.

Note that since we study only a single initial condition, we cannot rule out the appearance of multiple attractors, nor the existence of attractors that might occur for other initial points in the “unbounded” region of the figure. Indeed, we show in Fig. 6 the same parameter range as Fig. 5(a), but now choosing the initial point  $(x_0, x_{-1}, x_{-2}) = (0.0125839, 0.677585, -1.25765)$ . Note that there is a striking absence of the stable fixed point and its doubling sequence for  $r > 0$  and  $\alpha$  small as compared to Fig. 5. Moreover there is a new stable region (gold) corresponding to a period-3 attractor along with a small doubling-cascade to periods 6 and 12.

Figure 5(a) shows the range  $(\alpha, r) \in [-3, 0] \times [-0.75, 0.5]$ . The fixed point  $x_-$  is stable in the “strong blue” region, and undergoes a doubling bifurcation along the curve

$$(3r^2 - 4)^2 \alpha^2 + 2((5\delta^2 + 6\delta + 9)r^2 - 4\delta^2 + 8\delta + 12)\alpha + (\delta + 1)^2(\delta - 3)^2 = 0, \quad (33)$$

<sup>4</sup>In [HM22a], it was proved that all bounded orbits lie in the set  $|x| < \kappa$  for a given  $\kappa > 0$  depending upon the map parameters. We take  $\kappa_{max}$  to be the maximum value of  $\kappa$  over the parameters studied.

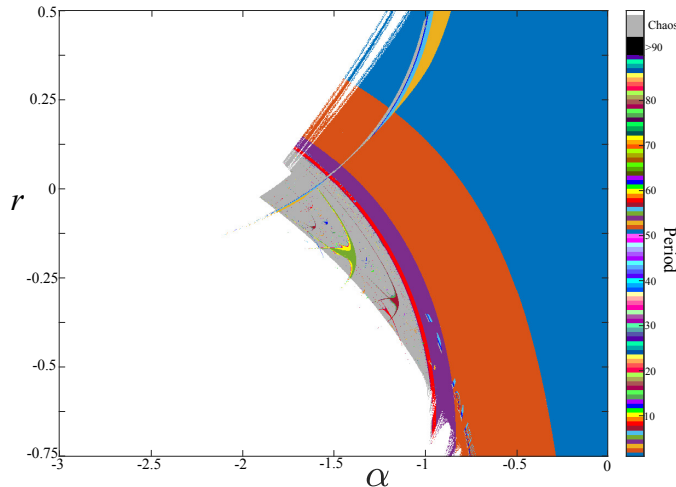


Figure 6: Bounded, periodic and chaotic orbits for case (SC) over the same parameter range as Fig. 5(a), but using a different initial condition. The new gold, period-3 attracting region not seen in Fig. 5(a) shows the possibility of multiple attractors.

to become a stable period-two orbit (vivid orange). Subsequent doublings as  $\alpha$  decreases create period-four (magenta) and period-eight (red) orbits.

An enlargement of the boxed region in Fig. 5(a) is shown in Fig. 5(b) for  $(\alpha, r) \in [-1.7, -0.9] \times [-0.375, 0]$ . Prominent features in this region are resonant “shrimps” including the period-five (dark green) and period-seven (dark red) cases. A shrimp is a codimension two structure much studied in two-parameter families of one and two-dimensional maps [Gal94, MT87, FOG13]. Within a period- $n$  shrimp, there is an attracting period- $n$  orbit and a partnered period- $n$  saddle. The “head” of the shrimp corresponds to a pair of curves of saddle-node bifurcations and the “tail” to sequences of period-doubling bifurcations. The endoskeleton of the shrimp is near the curve where the trace of the Jacobian is zero [FOG13]. As can be seen in the figure, shrimps swim in a “sea of chaos”.

To study the bifurcations in more detail, we set  $r = -0.18$ , seen as a line segment in Fig. 5. This segment enters the region of bounded orbits at  $\alpha = -1.541$ , crosses the dark green, period-five shrimp when  $-1.480 \leq \alpha \leq -1.381$ , and enters the doubling cascade of the fixed point at  $\alpha = -1.2031$ . In the following subsections, we will continue periodic orbits from  $\varepsilon = 0$  along this line using the numerical continuation algorithm discussed in Appendix C.

### 5.1 Low-Period Orbits and the Period-Doubling Cascade

There are 23 possible periodic symbol sequences with periods  $p \leq 6$ . Note that by §4.1, for the case (SC), when  $|r| < 2^{-1/2}$  there is a one-to-one correspondence between symbol sequences and AI states. The AI states can be easily found by iteration from an arbitrary point in the interval  $B$ , since the maps  $f_s$  (12) are contracting in this case. In this section we will continue each of these AI states for  $r = -0.18$ .

We expect that at least one period- $n$  AI state will continue to the  $\alpha$  range where there is a stable period- $n$  orbit seen in Fig. 5. This is in alignment with the “no-bubbles” conjecture proposed



in [SDM99]: every orbit of the map is continuously connected to the AI limit. Since the attractors in Fig. 5 are found with a specific initial condition, it is certainly possible that AI states continue beyond the  $\alpha$  range in the figure: there could be multiple attractors with basins that may or may not contain our chosen initial point.

The results of the continuation for orbits up to  $p = 5$  are shown in a bifurcation diagram, projected onto the  $\xi_t$ -axis in Fig. 7(a), with each periodic orbit labelled as its symbol sequence, given in the legend of the figure. Note that the fixed points  $\{\pm\}^\infty$  extend for the entire  $\varepsilon$  range shown in the diagram, but all of the higher-period orbits are destroyed by  $\varepsilon = 1.4$ ; the final observed bifurcation is the reverse period-doubling that destroys the period-two orbit  $\{-+\}^\infty$  when it collides with  $\{-\}^\infty$ . Notice that the AI states themselves, i.e., the orbits at  $\varepsilon = 0$  all lie on a set of finite points, or some Cantor-like set, which is in agreement with the intuition of Conj. 2 discussed above.

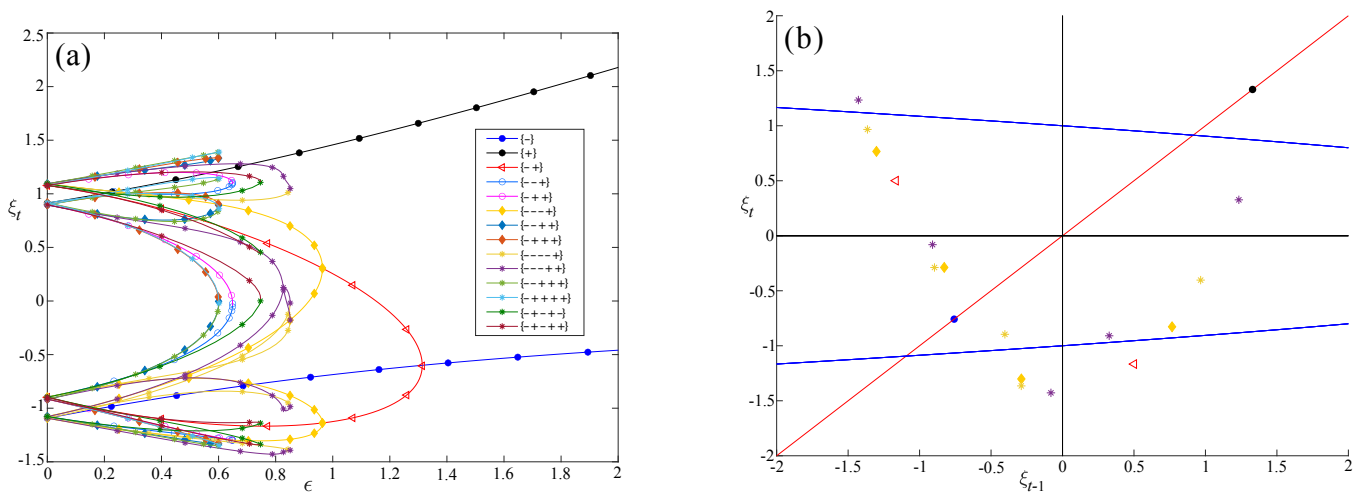


Figure 7: (a) Bifurcation diagram for low-period orbits up to period-five for case (SC) along  $r = -0.18$ . (b) 2D projection of orbits from (a) for the continuation step closest to  $\varepsilon = 0.8$ . Symbols for the orbits are the same as in (a). Included is the AI limit curve (9) (blue), which is a parabola for this case, and the diagonal (red) for reference.

The period-doubling and saddled-node bifurcations that are found by this process are summarized in Table 2. The fourth column of the table gives a 5-digit estimate of the bifurcation value, from the continuation algorithm. Analytically, using (33) for  $r = -0.18$  the fixed point doubles at  $\alpha_{PD} = -0.579494815477836$ . The computations continue to  $\alpha = -0.5794956$ , which differs by  $8(10)^{-7}$ . Since we have not used a bifurcation detection criterion in the continuation algorithm, we do *not* expect high accuracy for these values. Moreover, detecting bifurcations using multipliers can be problematic for  $\delta = 0.05$ : since the product of the multipliers of the linearization of (1) is its Jacobian determinant, then for a period- $n$  orbit,  $\lambda_1\lambda_2\lambda_3 = \delta^n$ . Implementation of such a detection criterion to compute  $\lambda = 1$  or  $-1$  requires high precision computations as  $n$  grows.

Note that in each case shown in Table 2, the codimension-one bifurcations occur between orbits with exactly one differing symbol. This agrees with our previous conjecture in [HM22b].

Both of the period-three orbits are destroyed by saddle-node bifurcations below the onset of the bounded attractors of Fig. 5, at  $(\alpha, r) = (-1.541, -0.18)$ . This agrees with the absence of period-three attractors along the line  $r = -0.18$ . Two of the three period-four orbits are similarly



Parent	Type	Child	$\varepsilon$	$\alpha$
$\{-\}^\infty$	pd	$\{-+\}^\infty$	1.3136	-0.5795
$\{-+\}^\infty$	pd	$\{- - - +\}^\infty$	0.9639	-1.0764
$\{- + +\}^\infty$	pd	$\{- - + + - +\}^\infty$	0.6478	-2.3843
$\{- - - +\}^\infty$	pd	$\{- - - + - + - +\}^\infty$	0.9220	-1.1763
	sn	$\{- \pm +\}^\infty$	0.6492	-2.3723
	sn	$\{- \pm ++\}^\infty$	0.6002	-2.7762
	sn	$\{- - - \pm +\}^\infty$	0.8510	-1.3808
	sn	$\{- + - + \pm\}^\infty$	0.7473	-1.7908
	sn	$\{- \pm + + +\}^\infty$	0.6017	-2.7622
	sn	$\{- - - \pm - +\}^\infty$	0.9266	-1.1648
	sn	$\{- - - \pm ++\}^\infty$	0.8007	-1.5597
	sn	$\{- + - + + \pm\}^\infty$	0.6889	-2.1070
	sn	$\{- \pm + + + +\}^\infty$	0.6005	-2.7734

Table 2: Parameters  $\varepsilon$  and  $\alpha = -\varepsilon^{-2}$  for period-doubling (pd) and saddle-node (sn) bifurcations for all orbits up to period six for the case (SC) with  $r = -0.18$ . Orbits are identified by their symbol sequences in the first and third columns. For saddle-node bifurcations, the symbol sequences of the two colliding orbits are listed together: the  $\pm$  indicates the single symbol that differs.

destroyed in a saddle-node, at  $\alpha = -2.7762$ , before the onset of bounded attractors. The remaining period-four orbit,  $\{- - - +\}^\infty$ , becomes stable in the magenta region of Fig. 5, and is destroyed by a (reverse) period-doubling of the  $\{-+\}^\infty$  orbit at  $\alpha = -1.0764$ . Only two of the period-five orbits continue into the bounded region,  $\{- - - \pm +\}^\infty$ ; these are the orbits that form the period-five shimp in Fig. 5. The attracting orbit has the sequence  $\{- - - + +\}^\infty$ ; the other,  $\{- - - - +\}^\infty$ , is a saddle. These orbits collide in a saddle-node bifurcation just as the line segment exits the shrimp at  $\alpha = -1.3808$ .

The pair  $\{- - - \pm - +\}^\infty$  of period-six orbits continues into the bounded orbit region and enters the period-doubling cascade of the fixed point. In the thin, soft blue strip seen in Fig. 5, the orbit  $\{- - - + - +\}^\infty$  is stable. In this region there is also an attracting period four orbit: this is a case of multiple attractors.

As Fig. 5 indicates, the fixed point  $\{-\}^\infty$  undergoes a period doubling cascade as  $\alpha$  decreases; the first doublings correspond to the symbol sequences shown in Table 3. These have a simple pattern if the sequences are properly ordered (as in Table 3): to get the sequence of period  $2^{n+1}$ , simply double that for period- $2^n$  and flip the first sign. This pattern is related to that found in [Hao91] for one-dimensional maps. This pattern also seems to hold for the doubling of the period-3 orbit, as seen in the third row of Table 2, if the period-3 orbit is first written as  $(+ - +)$ . This pattern was verified for a finite number of steps. Below we propose a formal conjecture.

**Conjecture 3.** *Symbol sequences between period-doubled periodic orbits of the map (1) have exactly one differing symbol. When written appropriately, the sequence of the doubled orbit is simply double that of the original orbit with the first sign flipped.*

In Fig. 7(b), the six orbits with  $p \leq 5$  that exist at  $\varepsilon = 0.8$  are projected onto the  $(\xi_{t-1}, \xi_t)$  plane. For these parameters, the line segment  $r = -0.18$  has not yet entered the region of bounded

Period	Sequence
1	$\{-\}^\infty$
2	$\{+(-)\}^\infty$
4	$\{- - (+-)\}^\infty$
8	$\{+ - + - (- - + -)\}^\infty$
16	$\{- - + - - - + - (+ - + - - - + -)\}^\infty$
32	$\{+ - + - - - + - + - + - - - - + - (- - + - - - + - + - + - - - + -)\}^\infty$

Table 3: Symbol sequences for the period-doubling cascade of the fixed point  $\xi_-$ .

attractors. Nevertheless this figure indicates that the low-period orbits appear to trace a horseshoe-like structure reminiscent of the Hénon attractor.

## 5.2 Hénon-like Attractors

When  $r = -0.18$ , chaotic attractors are indeed found when  $\alpha$  is in the gray regions of Fig. 5, just outside the period-five shrimp. One such attractor with  $\alpha = -1.25$  is shown in Fig. 8(a). Indeed, this is a chaotic attractor since, using the method described in [HM22a], its maximal Lyapunov exponent is 1.30116. To understand how this attractor develops, we first find a periodic approximation by iterating the point  $(-1.3387, -0.2563, -0.9553)$  on the attractor using map (1) until it exhibits a close return—within a distance of 0.005. The first three such close return times are listed in Table 4.

period	return distance	$\varepsilon$	$\alpha$
273	$7.96(10)^{-5}$	0.894	-1.250
423	$2.4(10)^{-3}$	0.894	-1.252
1200	$4.0(10)^{-5}$	0.893	-1.255

Table 4: Approximate periods and return distances for orbits on the chaotic attractor for  $(\alpha, r) = (-1.250, -0.18)$ . The last two columns show bifurcation values for orbits continued from the AI limit using the inferred periodic symbol sequences.

Using these orbits we can construct an associated symbol sequence under the assumption that

$$s_t = \text{sign}(\xi_t),$$

as it would be needed to use (12) at the AI limit. Thus each periodic approximation has a corresponding periodic symbol sequence, which we use to find an AI state. These are then continued away from  $\varepsilon = 0$ , again using the method described in Appendix C. The resulting orbits persist up to the values of  $\varepsilon$  shown in column three of Table 4. These orbits are shown at these maximal  $\varepsilon$ -values in Fig. 8(b,c,d). The period-273 approximation to the chaotic attractor persists the longest, reaching  $\alpha = -1.250$ . The two longer periodic approximations do not continue as far, even though the period-1200 orbit has a smaller return distance. In Fig. 9, there are six panels that follow the continuation solution over increasing  $\varepsilon$  of the period-1200 orbit (black) in  $(\xi_{t-1}, \xi_t, \xi_{t+1})$ -space. Also shown are the attractors (blue) as detected by the algorithm used to create Fig. 5. In Fig. 9(a), the period-1200 orbit is at the AI limit; it lies on a Cantor-like set. In Fig. 9(b,c),  $\varepsilon$  has not yet reached the region of bounded attractors, and the period-1200 orbit continues to evolve by growing apart

and onto a folded structure. Only Fig. 9(d) shows an instance where both the continued period-1200 orbit and an attractor co-exist; they appear to cover the same invariant set. For slightly larger  $\varepsilon$ , the period-1200 orbit is destroyed and, as seen in Fig. 9(e), the attractor has split into two chaotic bands. Effectively, these have “(reverse) merged” from the chaotic attractor that was seen in panel (d). These bands subsequently collapse in a (reverse) period-doubling cascade; the period-two case is shown in panel Fig. 9(f).

For reference we give the period-273 symbol sequence:

$$\{(-(+)^4 -^2 (+)^6 -^2 (+)^6 -^2 (+)^2 -^2 (+)^3 -^2 (+)^2 -^2 (+)^7 -^2 (+)^9 -^2 (+)^2 -^2 (+)^4 -^2 (+)^2 -^2 (+)^2 -^2 (+)^2 -^4 + -^3 (+)^2 -^7 (+)^3 -^8 (+)^3 -^2 (+)^5 -^2 (+)^2 -^2 (+)^3 + -^3 (+)^2 -^2 (+)^3 -^2 (+)^5 -^2 (+)^2 -^2 (+)^3 -^2 (+)^2 -^2 (+)^5 -\}$$

It is interesting that each subsequence of this orbit can be seen to be one of the sequences along the doubling cascade of the fixed point, i.e., from the list in Table 3. For example, in condensed form, the period-four orbit can be represented by either  $\{(+)^{-2}\}^\infty$  or  $\{+^{-3}\}^\infty$ , the period-eight orbit as  $\{(+)^3 -^2\}^\infty$ , etc. Chaotic attractors are often found after period-doubling cascades, so it seems apt that the symbolic sequence associated with a chaotic attractor is made up of such subsequences. It is interesting to speculate that one could predict the symbol sequence of such a chaotic attractor without a formal calculation of  $s_t$ .

## 6 Conclusions

In this paper we analyzed a two-parameter AI limit for the 3D quadratic diffeomorphism (1), extending our previous one-parameter results [HM22b]. To obtain an AI limit, we now assume that both  $\alpha$  and  $\sigma$  tend to  $\infty$ , adding the ratio  $\sigma^2/\alpha = -r^2$  as an additional parameter; our previous results assumed that  $\sigma$  remained finite so that only the single parameter  $\alpha$  went to infinity. In this new limit, the AI states are still determined by a one-dimensional correspondence (9), but the added parameter  $r$  shifts the center of the quadratic curve. To our knowledge, all previous studies of AI limits have been single parameter limits. There is still much to learn about how the different classes of AI limits—sending different parameters to infinity—transition from one to the other as parameters vary.

In §3, we generalized a result from [HM22b] to this case, obtaining a criterion for a one-to-one correspondence between symbol sequences and AI state, Lem. 1. Numerically computed parameter regions that satisfy the hypotheses of this lemma were found in §3.2. We observed that these regions seem to converge onto a region  $\mathcal{R}_A$ —simply defined by (15) and found in §4—that *can* be found analytically, recall (24).

In §5 we used numerical continuation from an AI state to obtain orbits of (1) as  $\varepsilon = 1/\sqrt{-\alpha}$  grows from zero. For the case that we study,  $b = c = 0$  in (1), so that the resulting diffeomorphism has just one quadratic term—it can be thought of as a 3D version of Hénon’s quadratic map. We chose the Jacobian of the map to be small,  $\delta = 0.05$ , so that the map is strongly volume-contracting. Thus this map is “close” to Hénon’s 2D map.

We studied the attractors of the map by looking at the trajectory of an initial condition near a fixed point of (1). When this trajectory remains bounded, it can limit to a periodic or chaotic attractor, and these were classified in Fig. 5 over a range of  $\alpha$  and  $r$ . We showed similar figures

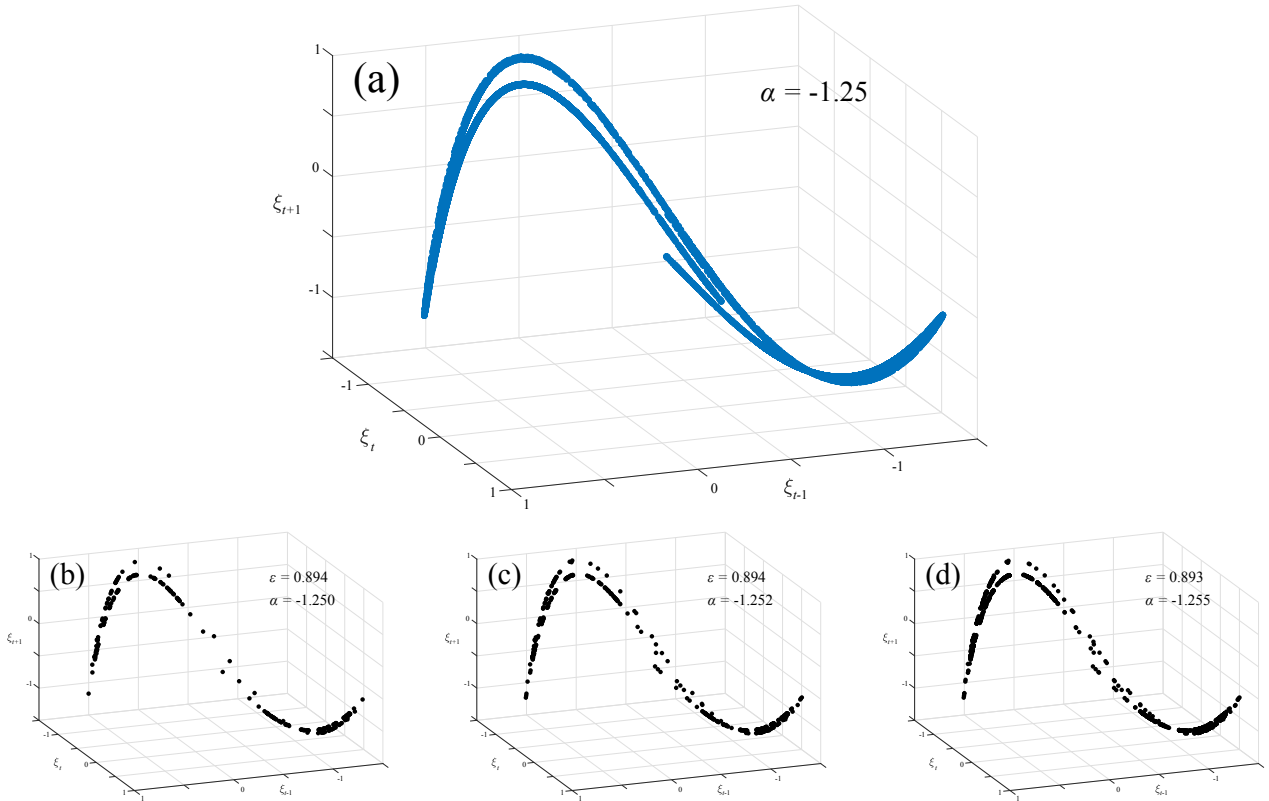


Figure 8: (a) The chaotic attractor at  $(\alpha, r) = (-1.25, -0.18)$  plotted in the rescaled spatial coordinates  $\xi = \varepsilon x$ . Continuation results for the period (b) 273, (c) 423, and (d) 1200 orbits that are obtained by close returns on the chaotic attractor. These are shown for  $\varepsilon$  given in the last column of Table 4.

for related parameter scans in [HM22a]. We observed that the low-period orbits that are stable in the “Arnold-tongues” of Fig. 5 correspond to orbits that are connected to those at the AI limit. We followed all the AI states up to period six, finding their codimension-one bifurcations in §5.1. These results are consistent with the, still unproven, “no-bubbles” conjecture for the 2D Hénon map [SM98]. Moreover, we observe that codimension-one bifurcations occur between orbits whose AI sequences differ in exactly one symbol; this is consistent with our previous results in [HM22b]. Similarly, we conjecture that the symbol sequences of orbits arising from period-doubling can be obtained from the parent orbit by doubling the sequence and then flipping exactly one symbol—the first, when ordered appropriately.

A deficit of our construction of Fig. 5 is that we followed only the fate of a single initial condition. However the map (1) can certainly have multiple attractors for fixed parameters. We observed this, for example, for a pair of period-six orbits that we followed from the AI limit: these continued into the period-doubling cascade of the fixed point, becoming stable in a parameter domain where there is also a stable period-four orbit. This is also seen in Fig. 6, which uses a different initial condition than that of Fig. 5(a), and clearly exhibits the existence different periodic attractors. One could speculate that continuation from the anti-integrable limit may be an efficient method to multiple attractors and those with small basins of attraction, as well as to find unstable orbits. We hope to

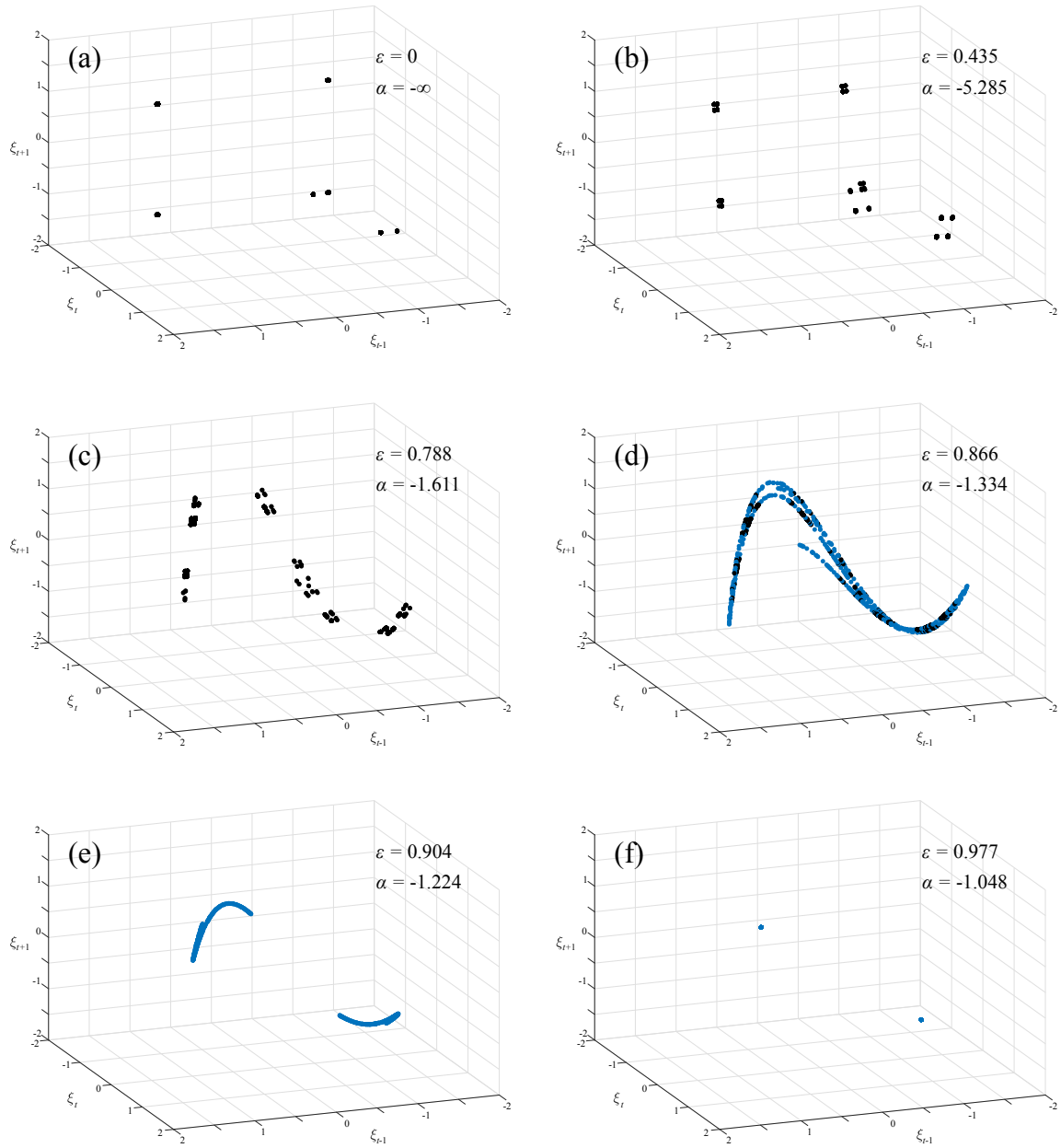


Figure 9: The continuation of the period-1200 orbit for six values of  $\varepsilon$  (black) in  $(\xi_{t-1}, \xi_t, \xi_{t+1})$ -space. Also shown are the attractors (blue) for the parameters with bounded orbits in Fig. 5. (a,b,c) The periodic orbit is unstable, before it enters the region of bounded orbits. (d) For  $\varepsilon = 0.866$ , the periodic orbit nearly coincides with a chaotic attractor. (e) Two chaotic bands that have (reverse) merged from the chaotic attractor seen in (d). (f) For larger  $\varepsilon$ , the attractor goes through a (reverse) period-doubling cascade, two examples of which are shown here. A movie showing these results as  $\varepsilon$  varies can be seen at [here](#).

explore this approach to explore multiple attractors in future research.

Note that even though we only detected orbits up to period 80 in Fig. 5, we did not find parameter values for which there is an attracting periodic orbit with larger period. This contrasts with some of the similar parameter scans in our previous work [HM22a]. We also do not observe attracting invariant circles for this strongly contracting case—these were seen for larger  $\delta$  in [HM22b, HM22a]. In the future, we hope to further investigate the symbol sequences for AI states that evolve to invariant circles. In particular, it would be interesting to see if there is a similar relation between symbols and rotation numbers as that found in the 2D Hénon case [DMS05]. Similarly, for the volume-preserving case, one could ask if there is a correspondence between symbols and the rotation vector for invariant tori.

## A Backwards Map

Here we compute the region  $\mathcal{R}_A^-$  of §4, imposing the condition (15) for the backwards AI map (21).

First suppose that  $\Delta = -4ac = 0$ . For the special case  $c = 0$ , the backwards map reduces to  $\xi_{t-1} = \frac{1}{r}(\xi_t^2 - 1)$ , a simple, deterministic, 1D map: there is no nontrivial AI limit. Thus when  $\Delta = 0$ , only the case  $1 - c = a = 0$ , where the curve (9) is a pair of parallel lines,

$$\xi_{t-1} = -\frac{1}{2}(r + s_t \sqrt{r^2 + 4}),$$

gives a nontrivial AI limit. In this case our arguments do apply using  $B$  (22) with  $\beta = \xi_{max}$  (26). The implication is that

$$\{(r, c) : c = 1\} \subset \mathcal{R}_A^-,$$

shown as the red line in Fig. 2(c).

For the ellipse,  $\Delta < 0$ , the map  $g_{\pm}$  has domain given by the vertical bounds of the rectangle (27) and range given by its horizontal bounds. Thus to satisfy  $g_{s_t}(B) \subset B$ , we set  $\beta = \frac{1}{2c}(|r| + \sqrt{r^2 + 4c})$  and require

$$\beta < \sqrt{\frac{r^2 + 4c}{4ac}}.$$

This parameter region in which this is satisfied is

$$\{(r, c) : \mathcal{C}_3(r) < c < 1\},$$

where  $\mathcal{C}_3$  the largest root of (25). This is the tan colored region in Fig. 2(c) and (d).

The hyperbolic case,  $\Delta > 0$  case requires a bit more work, as the backward  $\pm$  maps no longer have the up-down reflection symmetry of the forward map. Nevertheless we can still take  $B = [-\xi_{max}, \xi_{max}]$ . In order that the maps  $g_{\pm}$  are well-defined and give distinct orbits, the radicand of (21) must be positive,

$$r^2 + 4c - 4ac\xi_t^2 > 0.$$

When  $c > 1$ , so that  $a = 1 - c < 0$ , this is always true. Note that when  $c > 1$ , the asymptotes of the hyperbola (32) have a slope less than one when thought of as  $\xi_{t-1}$  as function of  $\xi_t$ . Thus  $g_{s_t}$  is a contraction on  $B$ . This implies that

$$\{(r, c) : c > 1\} \subset \mathcal{R}_A^-,$$

as shown in red in Fig. 2(c) and (d).

## B Parabolic Case: Two Iterates

For the case  $n = 2$ , we require  $\|D\mathcal{F}^2\|_{\infty} < 1$ . This will necessarily give a larger parameter interval,  $\mathcal{R}_2^+ \supset \mathcal{R}_1^+$ , since the product of two slopes can be less than one even when one of them is larger than one. The composition

$$f_{s_{t+1}}(f_{s_t}(\xi_{t-1})) = s_{t+1} \sqrt{r s_t \sqrt{r \xi_{t-1} + 1} + 1},$$

has derivative

$$f'_{s_{t+1}}(f_{s_t}(\xi_{t-1}))f'_{s_t}(\xi_{t-1}) = \frac{s_t s_{t+1} r^2}{4\sqrt{(r s_t \sqrt{r \xi_{t-1} + 1} + 1)(r \xi_{t-1} + 1)}}. \quad (34)$$

This has magnitude 1 when  $\xi$  is a root of the cubic polynomial

$$P_P(\xi_{t-1}) = 256r^5 \xi_{t-1}^3 + 256r^2(3r^2 - 1)\xi_{t-1}^2 + 32r(r^4 + 24r^2 - 16)\xi_{t-1} - r^8 + 32r^4 + 256r^2 - 256$$

Note that the discriminant of this polynomial,  $2^{16}r^{20}(64 - 27r^6)$ , is always positive on the interval  $|r| < \frac{1}{\sqrt{2}}$ ; thus the three roots of  $P_P$  are real. Thus to enforce the derivative (34) to have magnitude less than one, the roots must lie outside  $B$ . Numerically, this gives the bound

$$|r| \lesssim 0.6984177,$$

which is only a slight improvement over the case  $n = 1$ .

## C Continuation Algorithm

The persistence of AI states away from the AI limit can be proven using contraction arguments [SM98, HM22b]. Straightforward numerical continuation can be used for periodic orbits of (1). The continuation algorithm is based on reformulating the difference equation (6) to use a predictor-corrector method. A period- $n$  orbit, i.e., a sequence

$$\xi \in \{\xi \in \mathbb{R}^\infty \mid \xi_{t+n} \equiv \xi_t, \forall t \in \mathbb{Z}\} \simeq \mathbb{R}^n,$$

must be a zero of the function  $\mathcal{G} : \mathbb{R}^n \times \mathbb{R} \rightarrow \mathbb{R}^n$  defined by

$$\mathcal{G}(\xi, \varepsilon) = (\mathcal{L}_\varepsilon(\xi_1, \xi_0, \xi_{n-1}, \xi_{n-2}), \mathcal{L}_\varepsilon(\xi_2, \xi_1, \xi_0, \xi_{n-1}), \dots, \mathcal{L}_\varepsilon(\xi_0, \xi_{n-1}, \xi_{n-2}, \xi_{n-3})).$$

We use a standard pseudo-arclength continuation algorithm [KOGV07, Sec. 1.2.3], to find a discretization of a curve of solutions,  $\mathcal{G}(\xi, \varepsilon) = 0$ , at discrete points  $(\xi^k, \varepsilon^k) \in \mathbb{R}^n \times \mathbb{R}$ , for  $k = 0, 1, \dots$

Given a solution  $(\xi^k, \varepsilon^k)$  at index  $k$ , a direction vector,  $v^k = (\dot{\xi}^k, \dot{\varepsilon}^k)$ , and a predetermined arclength step size,  $\ell$ , the goal is to find a new solution in the hyperplane orthogonal to  $v^k$  at a distance  $\ell$  from the previous solution. Thus, to obtain  $(\xi^{k+1}, \varepsilon^{k+1})$ , one must solve the system

$$\begin{aligned} \mathcal{G}(\xi^{k+1}, \varepsilon^{k+1}) &= 0, \\ \dot{\xi}^k(\xi^{k+1} - \xi^k) + \dot{\varepsilon}^k(\varepsilon^{k+1} - \varepsilon^k) &= \ell. \end{aligned} \quad (35)$$

This can be done iteratively, beginning with the point in the hyperplane along  $v^k$ ,  $(\xi^{k+1}, \varepsilon^{k+1}) = (\xi^k, \varepsilon^k) + \frac{\ell}{\|v^k\|} v^k$ , i.e., as an initial guess. A solution to (35) is then obtained using Broyden's quasi-Newton method to approximate the Jacobian of (35) and a  $QR$ -decomposition to find its inverse [AG90]. In our computations, the Broyden iteration stops when  $\|\mathcal{G}\|_\infty < 10^{-12}$  or after a predetermined maximum number of steps, here set to 150.

The algorithm is initialized with an AI state,  $(\xi^0, 0)$ , which is found by iterating  $f_{s_t}$  (12) for the given period- $n$  symbol sequence  $s$ , beginning with a randomly selected point  $\xi_0 \in B$ , and then



iterating until the orbit converges to a tolerance of  $10^{-12}$ . The initial vector  $v^0 = (\xi^0, 0.005)$  is chosen so that  $\xi^0$  solves the first  $n$  rows of

$$\begin{pmatrix} \partial_\xi \mathcal{G}(\xi^k, \varepsilon^k) & \partial_\varepsilon \mathcal{G}(\xi^k, \varepsilon^k) \\ \dot{\xi}^k{}^T & \dot{\varepsilon}^k \end{pmatrix} \begin{pmatrix} \xi^{k+1} \\ \varepsilon^{k+1} \end{pmatrix} = \begin{pmatrix} 0 \\ 1 \end{pmatrix}. \quad (36)$$

Subsequently, each new direction vector  $(\xi^{k+1}, \varepsilon^{k+1})$  is found by solving the full system (36) to obtain a normalized tangent vector.

In addition to the mapping parameters  $a, c, r$ , and  $\delta$ , we choose an initial arclength step size  $\ell$ , which varies depending on the period  $n$  and values of the parameters. For periodic orbits with length less than 10, we chose  $\ell = 10^{-2}$ . For longer orbits, we chose  $\ell = 10^{-1}$ . During the continuation process,  $\ell$  is decreased by a factor of two if the solution is more than a distance of 0.1 from the previous solution (i.e., if the solutions jumps “too far away”). The continuation runs until  $\varepsilon$  ‘turns around’, i.e.,  $\varepsilon^{k+1} < \varepsilon^k$ , or until  $\ell$  becomes smaller than  $10^{-15}$ .

## References

- [AA90] S. Aubry and G. Abramovici. Chaotic trajectories in the standard map, the concept of anti-integrability. *Physica D*, 43:199–219, 1990. [https://doi.org/10.1016/0167-2789\(90\)90133-A](https://doi.org/10.1016/0167-2789(90)90133-A).
- [AG90] E.L. Allgower and K. Georg. *Numerical Continuation Methods: An Introduction*, volume 13 of *Computational Mathematics*. Springer, 1990. <https://www.springer.com/gp/book/9783642647642>.
- [Aub95] S.J. Aubry. Anti-integrability in dynamical and variational problems. *Physica D*, 86:284–296, 1995. [https://doi.org/10.1016/0167-2789\(95\)00109-H](https://doi.org/10.1016/0167-2789(95)00109-H).
- [Che06] Y.C. Chen. Smale horseshoe via the anti-integrability. *Chaos, Solitons & Fractals*, 28(2):377–385, 2006. <https://doi.org/10.1016/j.chaos.2005.05.050>.
- [CL15] Hung-Ju Chen and Ming-Chia Li. Stability of symbolic embeddings for difference equations and their multidimensional perturbations. *Journal of Differential Equations*, 258(3):906–918, 2015. <https://doi.org/10.1016/j.jde.2014.10.008>.
- [DLM06] B.-S. Du, M.-C. Li, and M.I. Malkin. Topological horseshoes for Arneodo-Coulet-Tresser maps. *Regul. Chaotic Dyn.*, 11(2):181–190, 2006. <https://doi.org/10.1070/RD2006v011n02ABEH000344>.
- [DM08] H.R. Dullin and J.D. Meiss. Nilpotent normal forms for a divergence-free vector fields and volume-preserving maps. *Physica D*, 237(2):155–166, 2008. <https://doi.org/10.1016/j.physd.2007.08.014>.
- [DMS05] H.R. Dullin, J.D. Meiss, and D. Sterling. Symbolic codes for rotational orbits. *SIAM J. Appl. Dyn. Sys.*, 4:515–562, 2005. <https://doi.org/10.1137/040612877>.

- [FOG13] W. Façanha, B. Oldeman, and L. Glass. Bifurcation structures in two-dimensional maps: The endoskeletons of shrimps. *Physics Letters A*, 377(18):1264–1268, 2013. <https://doi.org/10.1016/j.physleta.2013.03.025>.
- [Gal94] J.A.C. Gallas. Dissecting shrimps: Results for some one-dimensional physical models. *Physica A: Statistical Mechanics and its Applications*, 202(1):196–223, 1994. <https://www.sciencedirect.com/science/article/pii/0378437194901740>.
- [GGKS21] S.V. Gonchenko, A. Gonchenko, A. Kazakov, and E. Samylnina. On discrete Lorenz-like attractors. *Chaos*, 31(2):023117, 2021. <https://doi.org/10.1063/5.0037621>.
- [GMO06] S V. Gonchenko, J.D. Meiss, and I.I. Ovsyannikov. Chaotic dynamics of three-dimensional Hénon maps that originate from a homoclinic bifurcation. *Regul. Chaotic Dyn.*, 11(2):191–212, 2006. <https://doi.org/10.1070/RD2006v011n02ABEH000345>.
- [Hao91] Bai-lin Hao. Symbolic dynamics and characterization of complexity. *Physica D*, 51(1-3):161–176, 1991. [https://doi.org/10.1016/0167-2789\(91\)90229-3](https://doi.org/10.1016/0167-2789(91)90229-3).
- [HM22a] A.E. Hampton and J. D. Meiss. The three-dimensional generalized Hénon map: Bifurcations and attractors. *Chaos*, 32(11):113127, 2022. <https://doi.org/10.1063/5.0103436>.
- [HM22b] A.E. Hampton and J.D. Meiss. Anti-integrability for three-dimensional quadratic maps. *SIAM J. Appl. Dyn. Sys.*, 21(1):650–675, 2022. <https://doi.org/10.1137/21M1433289>.
- [JLM08] J. Juang, M.C. Li, and M.I. Malkin. Chaotic difference equations in two variables and their multidimensional perturbations. *Nonlinearity*, 21(5):1019–1040, 2008. <https://doi.org/10.1088/0951-7715/21/5/007>.
- [KOGV07] B. Krauskopf, H. Osinga, and G. Galan-Vioque. *Numerical Continuation Methods for Dynamical Systems. Understanding Complex Systems*. Springer, Berlin, 2007.
- [LLM99] K.E. Lenz, H.E. Lomelí, and J.D. Meiss. Quadratic volume preserving maps: An extension of a result of Moser. *Regul. Chaotic Dyn.*, 3:122–130, 1999. <https://doi.org/10.1070/RD1998v003n03ABEH000085>.
- [LM98] H.E. Lomelí and J.D. Meiss. Quadratic volume-preserving maps. *Nonlinearity*, 11(3):557–574, 1998. <https://doi.org/10.1088/0951-7715/11/3/009>.
- [LM06] M.C. Li and M.I. Malkin. Topological horseshoes for perturbations of singular difference equations. *Nonlinearity*, 19(4):795–811, 2006. <https://doi.org/10.1088/0951-7715/19/4/002>.
- [LM10] M.C. Li and M.I. Malkin. Approximation of entropy on hyperbolic sets for one-dimensional maps and their multidimensional perturbations. *Regular & Chaotic Dynamics*, 15(2-3):210–221, 2010. <https://doi.org/10.1134/s1560354710020097>.

- [MM92] R.S. MacKay and J.D. Meiss. Cantori for symplectic maps near the anti-integrable limit. *Nonlinearity*, 5:149–160, 1992. <https://doi.org/10.1088/0951-7715/5/1/006>.
- [MT87] R.S. MacKay and C. Tresser. Some flesh on the skeleton: The bifurcation structure of bimodal maps. *Physica D*, 27:412–422, 1987. [https://doi.org/10.1016/0167-2789\(87\)90040-6](https://doi.org/10.1016/0167-2789(87)90040-6).
- [SDM99] D. Sterling, H.R. Dullin, and J.D. Meiss. Homoclinic bifurcations for the Hénon map. *Physica D*, 134(2):153–184, 1999. [https://doi.org/10.1016/S0167-2789\(99\)00125-6](https://doi.org/10.1016/S0167-2789(99)00125-6).
- [SM98] D. Sterling and J.D. Meiss. Computing periodic orbits using the anti-integrable limit. *Phys. Lett. A*, 241(1/2):46–52, 1998. [https://doi.org/10.1016/S0375-9601\(98\)00094-2](https://doi.org/10.1016/S0375-9601(98)00094-2).